DYNAMICAL IMPACT OF THE MEKONG RIVER PLUME IN THE SOUTH CHINA SEA

A Dissertation
Presented to
The Academic Faculty

by

Xiyuan Zeng

In Partial Fulfillment
of the Requirements for the Degree
Master of Science in the
School of Earth and Atmospheric Sciences

Georgia Institute of Technology
May, 2021

DYNAMICAL IMPACT OF THE MEKONG RIVER PLUME IN THE SOUTH CHINA SEA

Approved by:

Dr. Annalisa Bracco, Advisor
School of Earth and Atmospheric Sciences
Georgia Institute of Technology

Dr. Takamitsu Ito
School of Earth and Atmospheric Sciences
Georgia Institute of Technology

Dr. Emanuele Di Lorenzo
School of Earth and Atmospheric Sciences
Georgia Institute of Technology

Date Approved: April 27, 2021

ACKNOWLEDGEMENTS

I am first and foremost thankful to my advisor Dr. Annalisa Bracco for guiding me carefully through these years. She has been a supportive mentor since my first entry to Georgia Tech. Without her contribution and encouragement, this thesis would not have been possible.

I would also like to thank my committee members for their help. Especially, I thank Dr. Takamitsu Ito for also being part of my qualifying exam committee and providing practical feedback to my comprehensive exam and research projects. I greatly appreciate the advice and assistance and the sharing of riverine discharge data from Dr. Joseph Montoya. The insightful comments and suggestions I received greatly improved this thesis.

Last but not the least, I thank my mom, dad, and friends for loving me no matter what happens.

TABLE OF CONTENTS

LIST OF FIGURES

SUMMARY

Near the ocean surface, river plumes influence stratification, buoyancy and transport of biological tracers, nutrients and pollutants. The extent to which river plumes influence the overall circulation, however, is generally poorly constrained. This work focuses on the South China Sea and quantifies the dynamical impacts of the Mekong River plume, which is bound to significantly change in strength and seasonality in the next 20 years if the construction of tens of dams moves ahead as planned. The dynamic changes induced by the freshwater fluxes introduced by the Mekong River are quantified by comparing submesoscale permitting and mesoscale resolving simulations with and without riverine input into the basin between 2011 and 2016.

In the summer and early fall, when the Mekong discharge is at its peak, the greater stratification causes a residual mesoscale circulation through enhanced baroclinic instability. The residual circulation is shaped as an eddy train with cyclones and anticyclones. Submesoscale fronts are responsible for transporting the freshwater offshore, for shifting eastward the development of the residual mesoscale circulation, and for further strengthening the residual eddy train. Overall, a greater northward transport characterizes the circulation in presence of riverine input. The significance of the mesoscale-induced and submesoscale-induced transport associated with the river plume is especially important in August and September, in the second half of the summer monsoon season, when primary productivity has a secondary maximum. Significant circulation changes, and therefore productivity changes, should be anticipated if the Mekong plume is modified by human activities.

CHAPTER 1 INTRODUCTION

1.1 Introduction of the South China Sea basin

The South China Sea (SCS), is the largest marginal sea in the Southeast Asia. It occupies the region from the equator to 23°N and from 99°E to 121°E (Hu et al. 2000) with a maximum depth of over 5000 m. Two broad shelves with depth shallower than 200 m are located on the northwestern and southwestern SCS, bordering the central, bowl-shaped deep basin.

The SCS circulation is strongly influenced by the monsoonal winds (Hellerman et al., 1983). In winter, northeasterlies prevail over the whole region with an average magnitude of 9 m/s and coastal upwelling off the coast of Vietnam is suppressed due to the wind-driven cyclonic circulation cell (Chao et al. 1996). In contrast, the weaker southwest summer monsoon winds from June to September, with average magnitude of 6 m/s, induce coastal upwelling that brings colder and saltier water to the surface (Wang et al., 2015). Two distinct circulation cells are also visible during this season (Dippner et al. 2011). The summer monsoon brings also intense rainfall over the ocean and Indochina, which in turn drives large pulses of riverine flow into the SCS via the Mekong River (Shaw and Chao 1994). The Mekong River, that originates in the Tibetan Plateau in China, drains a ~795,000 km^2 watershed and discharges into the SCS at the Mekong Delta in Vietnam with an annual mean flow of ~15,000 km^3/year (Pokhrel et al. 2018). The river plume contributes significantly to the hydrodynamics near and offshore its outflow points (Gonzalez et al. 2018), as a fresh offshore jet forms at about 12°N in late spring. The river water is then advected to the northeast by the monsoonal winds throughout the summer. The jet results from blockage of the southwest monsoon by the mountain range on the east coast of Indochina and is characterized by a strong intraseasonal variability in strength and extension (Xie et al., 2007). The path followed by the Mekong outflow differs between seasons: the river plume remains confined in the southward coastal jet during winter and spreads northwards over the shelf and then

off-shore in the jet in summer. Year around, the circulation in the basin is characterized by strong horizontal mixing, and sustained mesoscale activity (Gan et al. 2006, Cardona & Bracco 2012). The eddy field in summer and fall modulates the propagation of the river plume water and is especially energetic between 7ºN and 15ºN (Zhuang et al., 2020). The interplay between coastal upwelling, the jet, riverine (and nutrients) inflow and mesoscale circulations modulates, dynamically, phytoplankton communities and in turn primary productivity and fish abundance in the region (Weber et al., 2019), and controls the secondary peak in primary productivity observed between August and October (Liu and Chai, 2009).

Here, we explore the role of freshwater forcing on the SCS circulation using a regional ocean model. We focus on the dynamics associated to the river plume in boreal summer, and we explore its interaction with the jet and with the eddy train observed in this season (Nan et al., 2011; Chen et al., 2011; Zheng et al., 2014). The motivation for this work is the planned construction of 123 hydropower dams, including eleven hydropower plants hydropower dams along the Mekong River Basin and its major tributaries. The dams are expected to dramatically reduce the Mekong River mean, seasonal flow cycle (up to an order of magnitude) and sediment loading (Wild and Loucks, 2015). Studies on the environmental impacts have been limited so far to the land ecosystems and water resources (e.g. Yoshida et al., 2020 for an up-to-date analysis), but our results suggest that the overall circulation of the basin may be impacted as well.

1.2 The circulation in the SCS in boreal summer and fall

The South China Sea is the largest marginal sea in South Asia. It connects to the Sulu and Java Seas in the south through a number of shallow passages and with the Pacific Ocean through the deep (~ 2000 m) Luzon Strait in the north. Exchange of shelf waters between the South China Sea and the East China Sea occurs through the Taiwan Strait at a sill depth of 60 m.

As mentioned, the basin exhibits a strong, seasonally varying, wind-driven circulation

characterized by coastal upwelling and downwelling associated to monsoonal winds (Wyrtki et al., 1961). The southwest summer monsoon drives the circulation between May and September (Hellerman et al., 1983). Monsoonal winds make their appearance in the central portion of the basin in May and expand over the entire basin in July and August. In September, winds reverse to the northeast or winter monsoon phase north of 20°N, and the northeast monsoon expands southward in October, covering the entire South China Sea by December. April marks the end of the winter monsoon season.

In response to the changing winds a current develops off the coast of Vietnam. In Wyrtki's charts, in summer the current flows northeastward and the overall circulation pattern is an anticyclonic gyre. An important feature, significant along the northern boundary of the basin, is the Kuroshio intrusion through the Luzon Strait. Among the three passages along the eastern boundary, the Luzon Strait is the only opening where there is significant water exchange between the South China Sea and other basins. Water originating in the Pacific at depths between 1500 and 2000 m enters the SCS through the Luzon Strait and forms the deepest water mass of the basin (Nitani et al., 1972), moving southward into the basin along the western boundary (Shaw and Chao, 1994). In summer, two anticyclonic eddies appear to the southeast of the Zhongnan Peninsula and between the Xisha Islands and the Zhongsha Islands (Xu et al., 1982). Meanwhile, a cyclonic eddy, induced by the local summertime upwelling, forms to the east of the Vietnam coast and forces the main circulation to meander. Wu et al. (1998) suggested that the seasonal and inter-annual variations of the SCS circulation could be described by two modes in the velocity field. The first mode, associated with a southern gyre, shows symmetric seasonal reversal, being cyclonic in winter and anticyclonic in summer with limited year-to-year variations. The second mode, which contributes to the northern gyre off Vietnam, is responsible for the asymmetric seasonal and inter-annual variations. In general, in summer the cyclonic northern gyre and the anticyclonic southern gyre form a system with a jet among them that separates from the coast of Vietnam at 11°N ~ 14°N. The jet is responsible for the offshore transport of large pulses of Mekong River water.

The amount of river discharge varies in response to the monsoonal rainfall. Generally,

the Mekong River outflow remains low from February to June, increases from July onward, reaches its maximum around October, and decreases sharply after that. The Mekong outflow undergoes significant interannual variability. Over the period considered in this work, the Mekong outflow was strong in 2011, and only about ½ of the 2011 amount in 2015 and 2016, as a result of El Nino conditions. The El Nino Southern Oscillation (ENSO) indeed modulates the monsoonal winds, surface temperatures and precipitation over the SCS, and is associated to lower (higher) than normal summer rainfall in its positive (negative) phase in winter during peak ENSO conditions and in the following summer (Fan et al. 2018).

CHAPTER 2 MODEL SETUP, DOMAIN AND FORCING

2.1 Model setup, domain and forcing

We adopt the Regional Oceanic Modeling System-Coastal and Regional Ocean COmmunity model (ROMS-CROCO), a free-surface, terrain-following, hydrostatic, primitive-equation model (Marchesiello et al. 2009, Debreu et al., 2012). The model domain extends to the whole SCS at 5 km horizontal resolution (LR for Low Resolution) resolving the mesoscale circulation with a nested solution between 100°E-120°E and 3°N – 18°N at 1.6 km horizontal resolution (HR for Higher Resolution) that permits submesoscale circulations (McWilliams, 2016) to form (Figure 1). In the vertical there are 60 terrain-following layers with surface enhancement (no less than 20 layers in the upper 200 m in the deepest areas). CROCO is run from December 2009 to December 2016, after an opportune spin-up period in the LR configuration. The first year is discarded in the nested run and we focus on December 2010 onward in this work.

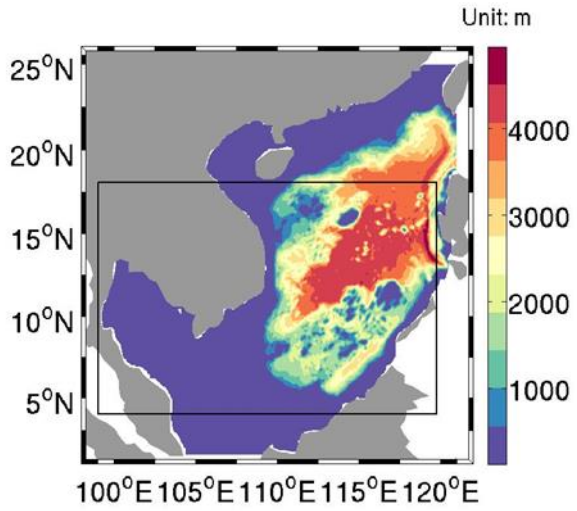

Figure 1 Model Domain and bathymetry. The whole map highlights the domain of the 5 km (LR) case. The black box encompasses the area where CROCO is run at horizontal resolution of 1.6 km (HR).

The model bathymetry is interpolated from ETOPO2 (Sandwell and Smith 1997) and

smoothed with a maximum allowed slope of 0.3. The parent grid simulation is forced by 6-hour surface wind stresses and daily heat fluxes from the European Centre for Medium-Range Weather Forecast ERA-5 reanalysis (Hersbach et al. 2020). Initial and boundary conditions are extracted from the Simple Ocean Data Assimilation (SODA), Version 3.4.2 dataset. The nested simulations with 1.6 km horizontal resolution use initial and boundary conditions interpolated from the 5 km horizontal resolution case, and same heat and momentum forcing from ERA-5. In order to explore the impact of the riverine input on the circulation of this basin, we perform simulations with and without riverine input for both resolutions. The with and without river cases for the 5 km and 1.6 km horizontal resolution run are indicated by LR-WR, LR-NoR, NoR and WR, respectively, here after, and we analyze in more detail the NoR and WR simulations.

Whenever the riverine forcing is included, the daily freshwater discharge from the stations of CanTho and Mythuan (Figure 2) is converted to an equivalent surface freshwater flux that decays exponentially away from the river mouths with a constant rate at each resolution (see Barkan et al., 2017 for a similar implementation strategy in the Gulf of Mexico). To isolate the impact from the fresh signals, no further salinity nudging is performed. The NoR case has the southern salinity boundary condition modified in order to remove the strong western boundary fresh signal that originates from east of Malaysia due to the Mekong riverine water accumulating in the shallower portion of the Gulf of Thailand.

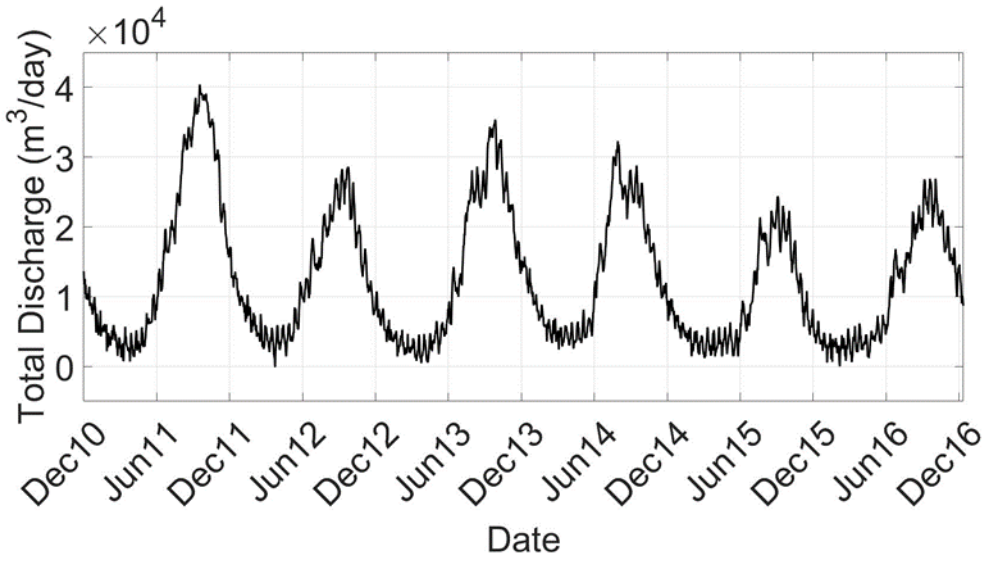

Figure 2 Timeseries of the Mekong River outflows from year 2010 to 2016. Unit: m^3/day.

2.2 Model validation

The mixed layer depth (MLD) is an important indicator of model realism given the processes we are interested in. We calculated the MLD using both a temperature criterion and a density criterion (Montégut et al., 2004). MLD_T is often defined as the depth at which the temperature differs from that at the surface by 0.2 ^oC, while MLD_ρ is commonly defined as the depth at which the density differs from the surface by 0.03 kg/m^3. The MLD_T time series in Figure 4 (a) are calculated for the whole domain and both WR and NoR integrations from 2011 to 2016. The MLD_ρ annual cycle (not shown) shares similar trends with a small difference in the magnitude of the changes and larger differences among the two runs. The MLD_T reaches its minimum in April, when the heat fluxes are strongest and the riverine discharge is at its minimum, and is deepest around December and January.

The model captures well the MLD_T variability. A secondary peak around July that can observed in 2012, 2013 and 2014 is also represented. Overall, the WR case has a slightly shallower MLD_T compared to NoR. The difference is small in late winter to spring, and more distinct during the months characterized by strong riverine discharge（Figure 3). The model underestimates the MLD in winter compared to SODA reanalysis, especially

in 2013. We do not have in-situ data in the area we are interested in to verify if this is a bias in CROCO or it results from a submesoscale-induced restratification of the water column in winter (Yu et al., 2019) that cannot be captured by SODA due to its coarser resolution. Obviously, differences between the upper stratification in WR and NoR are even larger if density is considered and the salinity signal is accounted for (not shown).

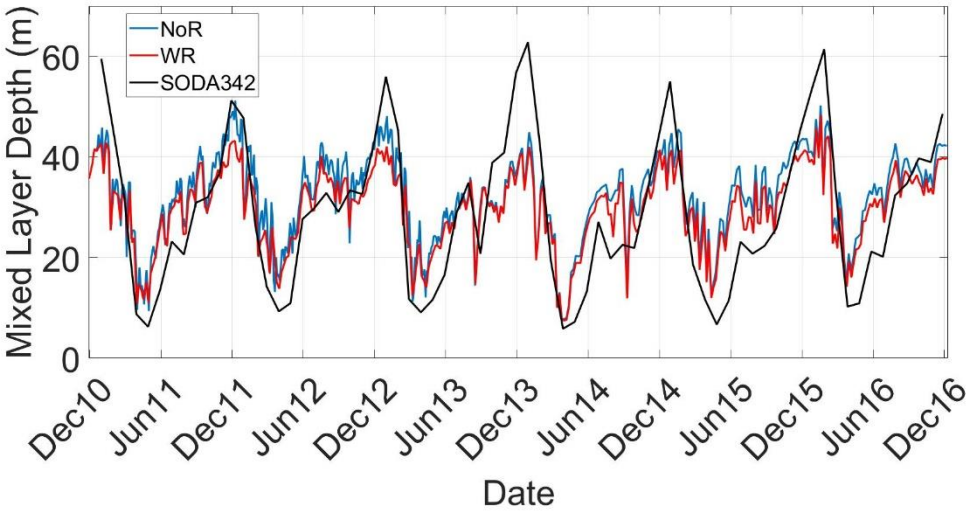

Figure 3 Mixed layer depth timeseries comparison among NoR, WR and SODA 3.4.2 calculated over the whole 1.6 km domain from year 2011 to 2016 using a temperature criterion (δT= 0.2°C).

CHAPTER 3 MODELED CIRCULATION

As mentioned, the circulation along the Vietnam coast is impacted by both the monsoonal winds and riverine discharge. The SCS western boundary current (SCSwbc) is a main contributor for the redistribution of water properties, momentum, energy and nutrients. The current is mainly wind-driven (Liu et al., 2001), and influences the regional climate (e. g., Xie et al., 2003; Zhou et al., 2010).

In boreal summer, the SCSwbc flows from the Karimata Strait northward along the southern Malay Peninsula, passes by the Gulf of Thailand and flows along the southeastern Vietnamese coast. The monsoonal winds transport the river plume northeastward, forming a jet of fresh water, and excite strong coastal upwelling near the coastline of Vietnam from 9°N to 12°N. When the summer SCSwbc reaches approximately 11◦N, it bends to the east forming the so-called Southeast Vietnam Offshore Current (VOC, Fang et al., 2002). The exact position of the VOC separation from coast varies among years between 10◦ and 14◦N (Figure 4).

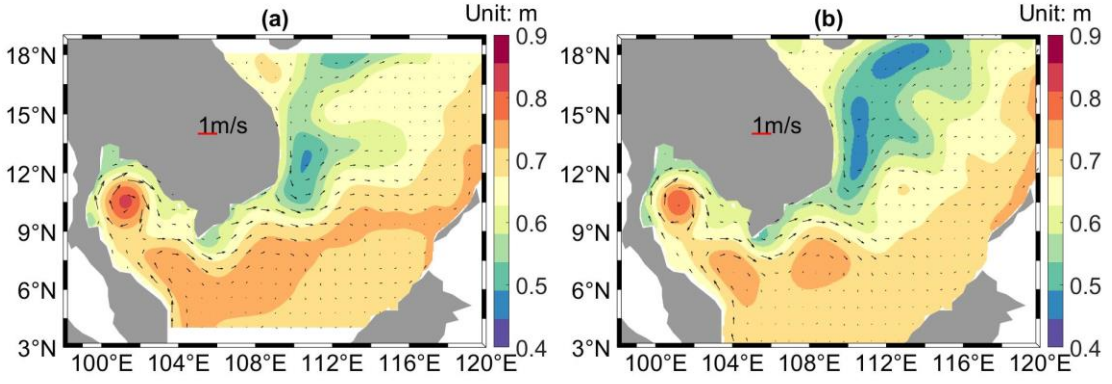

Figure 4 Sea surface high (SSH) field with superpose the surface velocity field averaged over June to October and 2011-2016 in the (a) WR and (b) LR-WR integrations.

The upwelling associated with the VOC leads to intense, negative temperature anomalies that extend to the upper 30-40 m of the water column. Figures 5 and 6 show SSH anomalies, and temperature and salinity snapshots at 15 meters depth for the WR and LR-WR runs in June and August 2012.

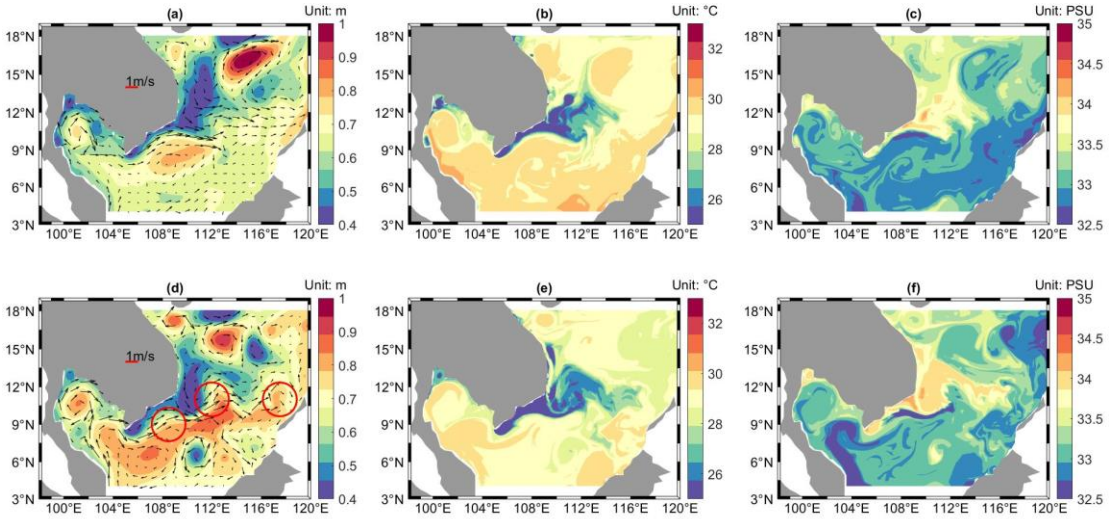

Figure 5 SSH anomalies (left), temperature (center) and salinity (right) snapshots in June 15 and August 14, 2012 in the WR simulation. Temperature and salinity are shown at 15 m depth. The anticyclonic eddy train is also indicated in the August snapshot.

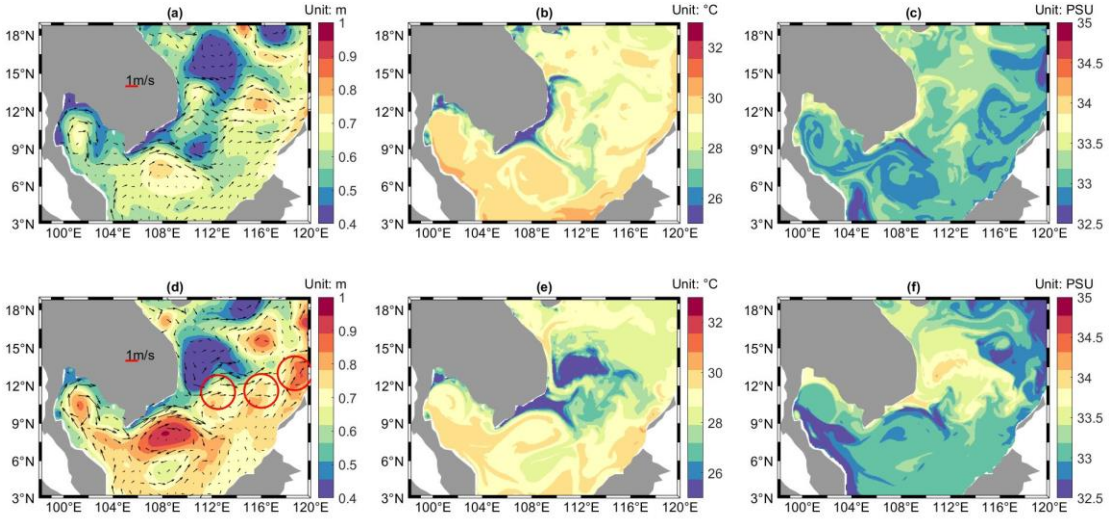

Figure 6 SSH anomalies (left), temperature (center) and salinity (right) snapshots

in June 15 and August 16, 2012 in the LR-WR simulation. Temperature and salinity are shown at 15 m depth. The anticyclonic eddy train is also indicated in the August snapshot.

In June, the SW monsoon induces coastal upwelling bringing colder and saltier water to the surface. The riverine signal penetrates eastward from June to August with interannual differences in timing and location. As the Mekong River discharge further increases and the monsoonal winds begin to change direction in September, the fresh anomalies propagate into the southwestern shallow shelf in fall.

The season mean and instantaneous snapshots of the modeled SSH in Figure 4-6, point also to the mesoscale structures that populate the SCS offshore the Vietnam coast. Both the WR and LR-WR simulations reproduces reasonably well the shape and position of the *eddy pair*, an anti-cyclonic southern recirculation and a cyclonic northern recirculation that form every year at the end of spring off eastern Vietnam around 10-12°N, 110-114°E, which signature is apparent also in the temperature and salinity distributions. The anticyclonic eddy has a warm and low salinity core, while the cyclonic eddy has a cold and salty core (Chen et al. 2010). The northern eddy (called East Vietnam Eddy, hereafter EVE), generally characterized by a narrow belt of low dynamic height east of Vietnam, is present in summer (June–August), and tends to strengthen toward the end of the season when prevailing winds are from the southwest (October–November). This cyclonic circulation persists in winter, until the monsoonal transition from the northeast to the southwest (March–May) (Qu et al., 2000). Over summer, months long-lived anticyclonic eddies (up to three) form along the jet while it meanders bringing the river plume water offshore, extending west to east (see Figure 5 and 6 for the SSH evolution from June to August). Cai and Gan (2017) used an idealized circular basin model to show that the anticyclonic eddy train originates from the separated jet and its downstream meandering, and that the stratification modulates intensity and vertical extension of the anticyclones. They analyzed the vorticity balance and found that its formation is favored by stratification.

CHAPTER 4 FRESHWATER DEPENDENCE

4.1 Horizontal density gradient and frontal tendency

Freshwater anomalies are transported offshore to the deep portion of the basin by a joint effort of the VOC and mesoscale eddies. These anomalies in turn modify the surface stratification. Additionally, near the Vietnam coast and along the jet, the riverine input enhances submesoscale activity and generates fronts that further promote the freshwater advection (Luo et al., 2016). In the following, we consider the dynamical evolution of quantities such as density gradients and frontogenesis during the summer monsoon season, comparing the runs with and without riverine forcing. We focus especially on the August to October period, when the freshwasher input in the SCS is largest.

In our submesoscale permitting simulations, the seasonal evolution of lateral density gradients $|\nabla_h \rho|$ is exemplified in Figure 7 where snapshots and the time-series of the mean annual cycling are presented for the WR and NoR runs. In the WR case, surface density gradients are greatest in fall, followed by summer, winter and spring. The seasonal cycle of $|\nabla_h \rho|$ follows that of the riverine input that increases from summer to late fall and decreases from the end of December into spring, with a minimum in early February. $\nabla_h \rho$ maps in NoR and WR are similar in winter when the riverine input is small and the monsoonal condition favors downwelling (not shown), but quite different in summer (Figure 7 (a) to (b)). The summer $\nabla_h \rho$ values in the NoR run, which are higher than in other seasons, are due to the coastal upwelling of cold and salty water to the surface and to the mesoscale eddies. The much larger $\nabla_h \rho$ in WR, on the other hand, is dominated by the introduction and offshore extension of the freshwater plume.

The extension reaches further offshore in the higher resolution case, through the advection of density anomalies into submesoscale fronts (Figure 7d), which contribution is strongly underestimated (close to zero) in the LR-WR case (Figure 8).

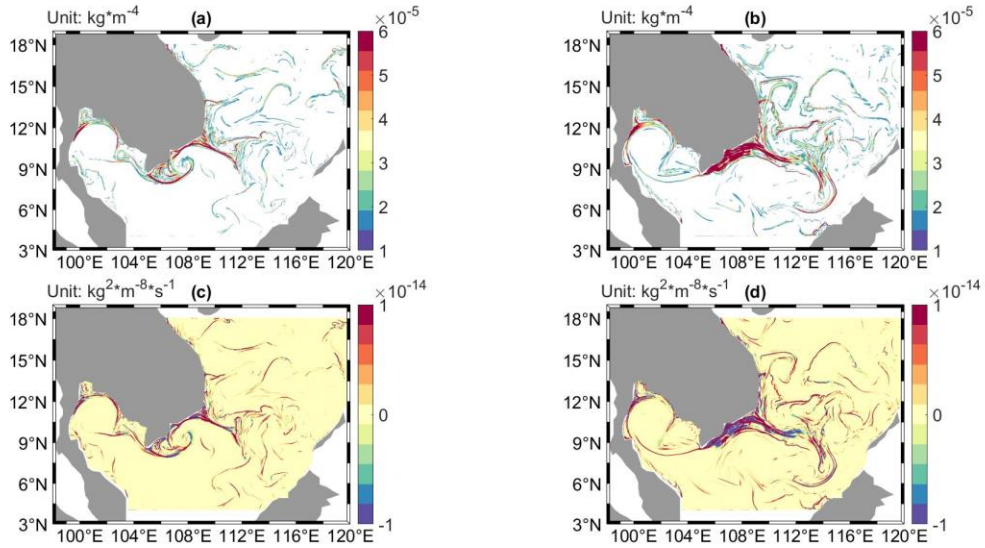

Figure 7 Instantaneous snapshots of horizontal density gradients, unit: kg m^{-4}, in August, 2014 in the (a) NoR, (b) WR. Instantaneous snapshots of frontal tendency, unit: kg^2 m^{-8} s^{-1}, in August, 2014 in the (c) NoR, (d) WR.

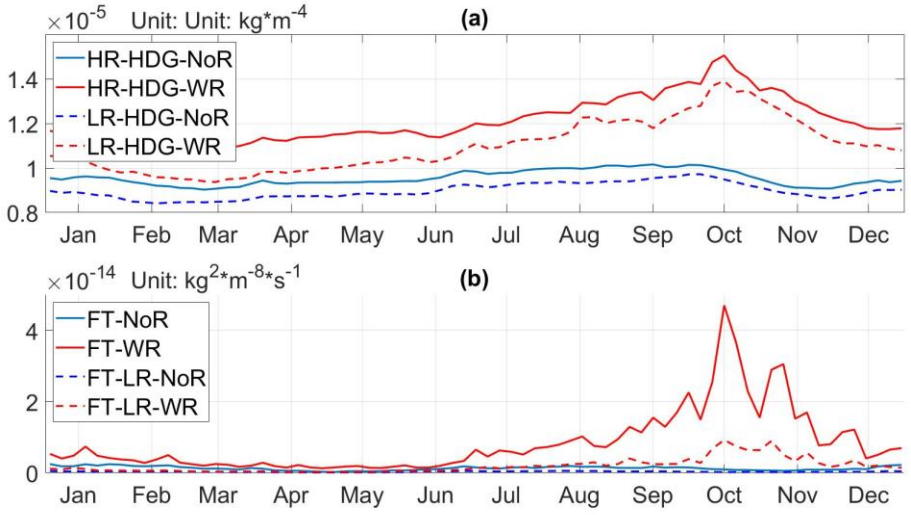

Figure 8 Annual cycle of (a) horizontal density gradients, unit: kg m^{-4} and (b) frontal tendency, unit: kg^2 m^{-8} s^{-1} in the WR (red, solid), LR-WR (red, dashed), NoR (blue, solid) and NoR-WR (blue, dashed) simulations. The time-series are constructed using 5-day averages over the whole domain and integration period 2011-2016.

The flow frontal tendency, F, defined as $F = \frac{D|\nabla_h \rho|}{Dt} = Q \cdot \nabla_h \rho$ with $Q = (Q_1, Q_2) = -$

$(\frac{du}{dx}\frac{d\rho}{dx}+\frac{dv}{dx}\frac{d\rho}{dy}+\frac{dv}{dy}\frac{d\rho}{dy})$ (Capet et al. 2008c; Hoskins 1982; Hoskins and Bretherton 1972) describes the evolution of the density gradients (i.e. their tendency to increase or decrease). A positive frontal tendency indicates an increase of the magnitude of the density gradients over time and therefore frontogenesis, while a negative sign implies frontolysis. A frontal jet tends to be confluent and frontogenetic on the upstream side of a meander trough and diffluent and frontolytic on the downstream side of it (Bower et al., 1989; Thomas and Joyce 2010). On the upstream side, frontogenesis is triggered by the straining of the horizontal flow, resulting in strongly positive *F*. On the downstream face, smaller-scale fluctuations related to small-scale meandering of the fronts occur, leading to mostly negative *F* (Gula et al., 2016). The seasonal evolution of *F* in WR follows closely that of the density gradients. It peaks in October, at the time when lateral density gradients are strongest, and has its minimum between March and May, when the discharge is small and the intrusion of cold salty water from the north is absent. In the LR-WR run the underestimation of submesoscale induced frontogenesis limits the offshore propagation of the plume water and its variability in time.

The presence/absence of water of riverine origin offshore influences the near-surface stratification and in turn the mesoscale circulation in the basin between, especially, August and October. Figure 9 shows the difference in sea surface heigh, horizontal velocity and stratification between the WR(LR-WR) and NoR(LR-NoR) simulations averaged over the six years considered and for August-to-October. Here the upper ocean stratification is defined by the density at 100-meter depth minus the density at 5-meter depth.

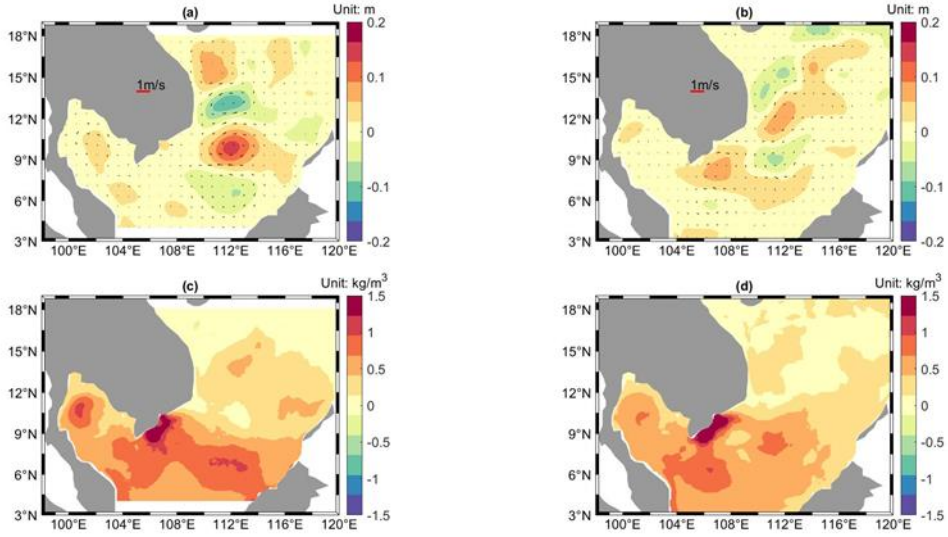

Figure 9 Differences in the mean of 2011 to 2016, August-to-October of (a-b) SSH with geostrophic velocities superposed, and (c-d) stratification (see text for definition) in the submesoscale permitting case (left) and in the LR simulations (right).

4.2 Residual eddy train

Independently of resolution and of the presence/absence of the Mekong freshwater fluxes, CROCO reproduces the eddy dipole structure and the EVE strengthening over the summer. The lack of accumulation of fresh and warm water near 10°N - 113°E in the NoR simulations, however, causes the offshore velocity to extend straightly eastward from 109°E to 112°E at around 9°N. The difference in SSH between WR and NoR runs has a noticeable wave (cyclonic-anticyclonic-cyclonic-anticyclonic) pattern east of the Vietnam coast with its strongest amplitude in September in all years, resulting in a greater northward component for the offshore velocity near 112°E. Among the residual mesoscale eddies, the clockwise residual eddy (here after CRE) centered around 10°N east off the coast is responsible for the stronger northward current around (11°N, 110°E) in WR. In the LR case the limited off-shore reach of the Mekong plume water implies smaller stratification differences away from the coast and a more coastally confined mesoscale residual.

Figure A1 shows the time evolution of the modeled mean SSH and velocity anomalies of year 2011 to 2016 from June to October in the higher resolution solutions. The typical pattern of the residual eddy train appears in June. From June to August, as the eddy dipole becomes more and more mature due to stronger SW monsoon and riverine input, the residual eddy train strengthens. This trend continues in September, despite a weakening of the SW monsoon winds, give that the river discharge continues to increase, and the eddy train moves slightly to the south. With the onset of the NE monsoon in October and the reversal of the winds, the northern anticyclonic-cyclonic patterns weaken.

In agreement with the idealized simulations in Cai et al. (2017), the residual eddy train is linked to differences in the upper stratification in the SCS and its signature in the full SSH field is towards a strengthening of the anticyclones that develop in summer as shown in Figure 2. The change of size and magnitude, as well as the movement of the anticyclonic-cyclonic-anticyclonic pattern follows that of the riverine input which is transported according to the monsoon winds. Overall, the combined effect of topography and stratification drives the development of the residual eddies, among which the CRE is the major contributor (Figure 10).

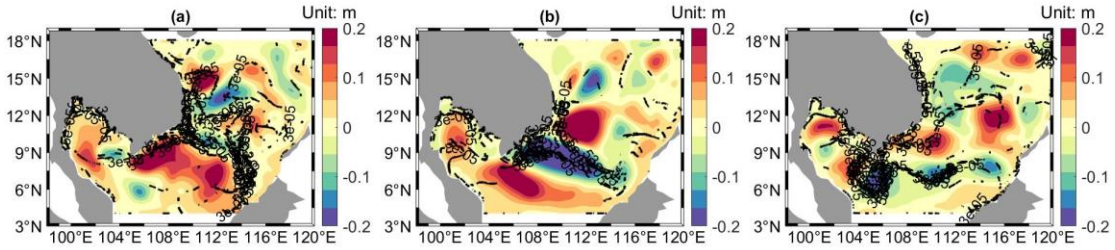

Figure 10 Differences in the mean (a) August, (b) September and (c) October, 2014 SSH between WR and NoR with superposed the WR lateral density gradient

contours on August 16, September 15 and October 15, 2014 comprised between $3x10^{-5}$ and $5x10^{-5}$ kg m^{-4}.

4.3 Zonal and meridional velocity and volume transport

Differences in mean lateral velocity averaged latitudinally over the area (9°N, 110°E) to (13°N, 115°E) from August to October, are shown in Figure 11 for the zonal and meridional components separately. The difference shows an enhancement of eastward momentum in WR. The largest difference, up to 0.15 m/s, is found in October, when the magnitude of the freshwater flux is strongest and when the monsoon brings colder and saltier water from the Hainan province that pushes the fresh signals "back" into the area considered, followed by August, when the summer monsoon winds can push the near-surface water offshore more easily in presence of a shallower mixed-later in WR. The meridional component differences vary with longitude and throughout the season, with an overall stronger northward current in WR in each of the years considered and with a core extending to the base of the mixed-layer at about 40 m of depth. The magnitude of the meridional difference is largest in September.

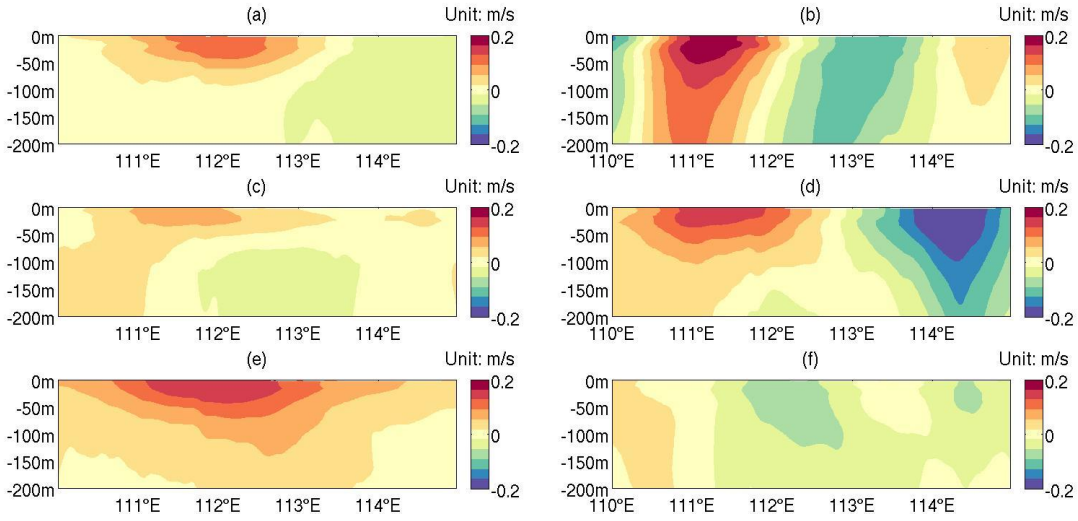

Figure 11 Difference in zonal (left) and meridional (right) velocity components (WR – NoR) latitudinally averaged in the area (9°N, 110°E) to (13°N, 115°E) in August (a-b), September (c-d) and October (e-f). Unit: m/s.

Finally, we computed the east-west (EW) and north-south (NS) volume transport at 12°N, integrating the velocities at the given section following Sanchez-Roman et al. (2018) (Figure 12). In presence of riverine input, the EW volume transport in the transect considered is predominantly eastward and more surface confined in WR.

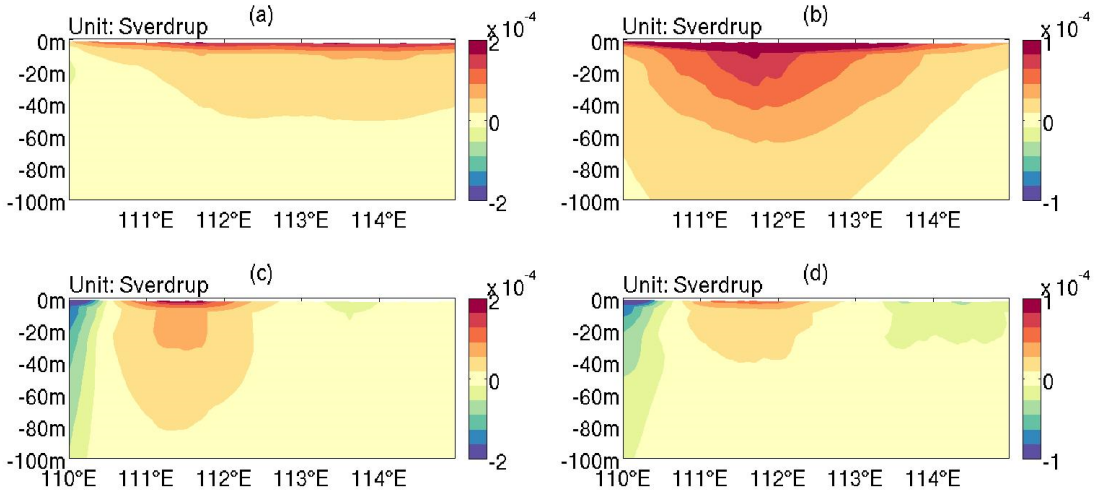

Figure 12 East-west (a-b) and north-south (c-d) volume transport across a transect at 12°N in WR, and the WR-NoR difference averaged over August-to-October. Unit: Sverdrup.

The warm and fresh water brought from the coast to 12°N, leads to higher SSH and stronger divergence, and a reduction in the westward volume transport found in the absence of riverine forcing. In the meridional direction, the volume transport in WR has a significantly stronger northward component, especially in August and September, close to the surface.

CHAPTER 5 CONCLUSIONS

Through a modeling exercise we have quantified the dynamical impact of Mekong River plume on the SCS circulation during the summer and early fall seasons. We have shown that the changes in stratification caused by the freshwater fluxes are responsible for a residual eddy train. The residual mesoscale circulation emerges in June and strengthens until August, to disappear with the monsoon wind reversal by the end of October.

A comparable impact of freshwater inputs on the overall circulation was found in the Caspian Sea (Kara et al., 2010). In that case, the simulation performed with no river discharge still produced the observed seasonal variation in surface circulation in the Caspian Sea, but resulted in a decrease in intensity of the southward current along the western coast of the central Caspian Sea, impacted by the Volga River. In the SCS, on the other hand, the summer 'gyres' and coastal currents are wind driven and alongshore coastal currents are not significantly modified. The freshwater-induced mesoscale anomalies, however, introduce a northward shift in the surface jet that forms offshore the Vietnam coast. The jet meanders and is more prone to baroclinic instability due to the increased stratification whenever influenced by the riverine input, in agreement with the idealized work by Cai and Gan (2017). Such northward component in the jet velocity is indeed observed in satellite SSH maps, and is greatly underestimated if the river fluxes are neglected.

Furthermore, we explored the role of submesoscale circulations and more broadly model resolution in the representation of the dynamical feedbacks of the riverine input in the SCS. By comparing mesoscale resolving runs at 5 km horizontal resolution with submesoscale permitting simulations at 1.6 km horizontal resolution, we found that submesoscale fronts greatly contribute to the offshore transport of freshwater anomalies and, in doing so, to the stratification patterns. The end result is an eastward, offshore shift of the residual eddy train in the solution at higher resolution.

Overall, our results point to the need to include ocean circulation changes - and in turn

primary productivity changes being the Mekong River a major supplier of nutrient, nitrogen and phosphorus among others (Weber et al., 2019) - to the list of environmental impacts associated with the construction of over 100 hydropower dams along the Mekong River Basin and its major tributaries.

We note that the investigation performed, while realistic, did not include tides, which may enhance mixing in this basin, and likely underestimated the Mekong plume impact by imposing the freshwater fluxes as salinity anomalies, therefore neglecting their contribution to the momentum flux. We plan to further explore those aspects in the near future.

APPENDIX A. FIGURES

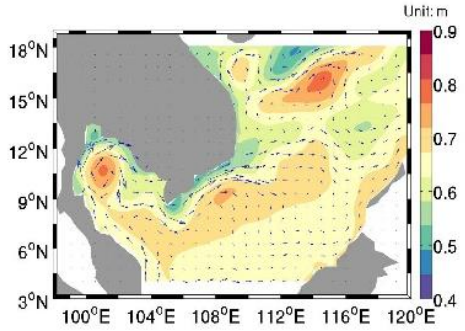

(a)

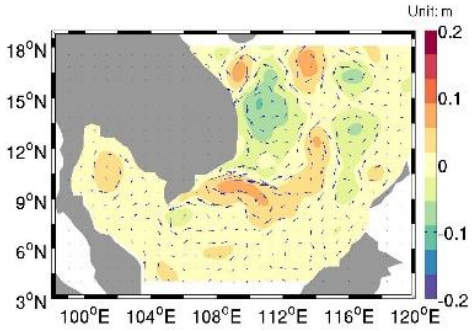

(b)

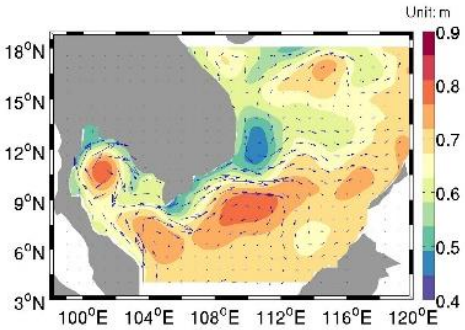

(c)

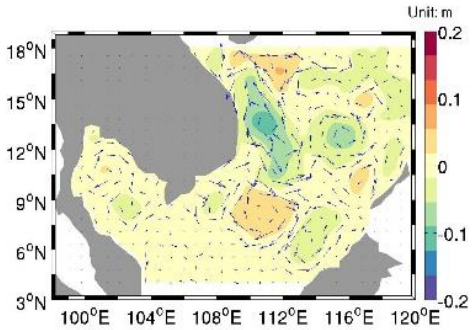

(d)

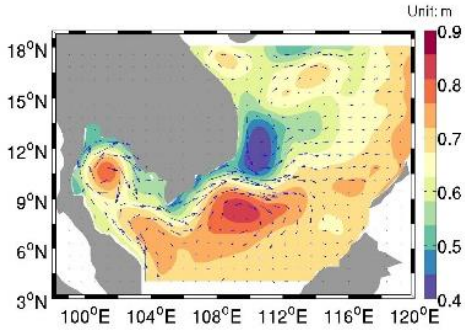

(e)

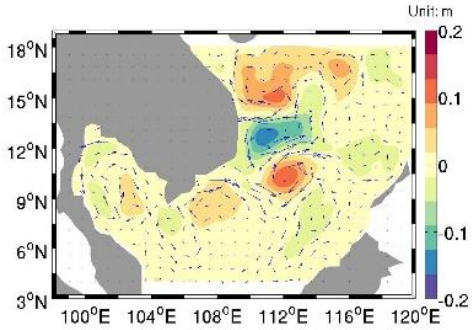

(f)

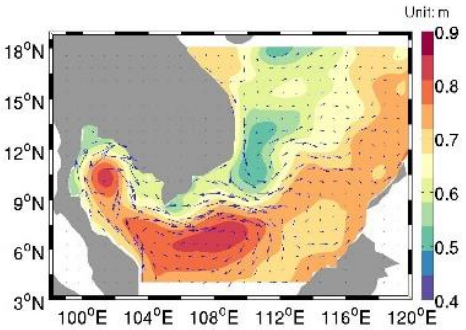

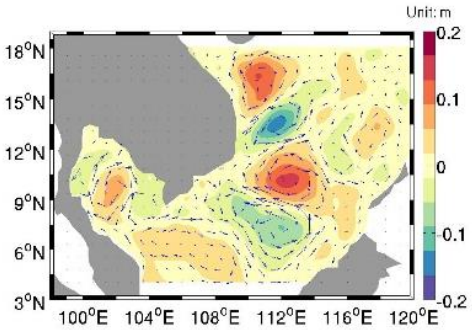

(g) (h)

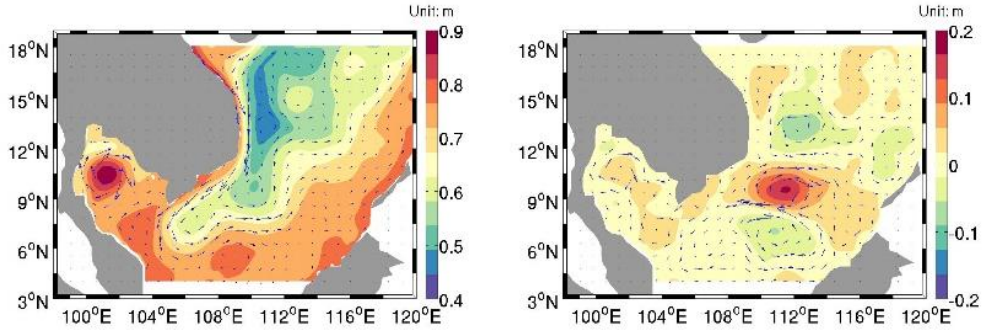

(i) (j)

Figure A1 Time evolution of modeled mean SSH and surface velocity averaged over the 2011-2016 period from June to October in the WR simulation(left) and the (WR-NoR)difference (right) in June (a-b), July (c-d), August (e-f), September (g-h) and October (i-j).

REFERENCES

A. Birol Kara, Alan J. Wallcraft, E. Joseph Metzger, Murat Gunduz. 2010. Impacts of freshwater on the seasonal variations of surface salinity and circulation in the Caspian Sea. Continental Shelf Research 30 (2010) 1211–1225.

Amy S. Bower. 1989. Potential Vorticity Balances and Horizontal Divergence along Particle Trajectories in Gulf Stream Meanders East of Cape Hatteras. Journal of Physical Oceanography Volume 19: Issue 11.

A. Wang, Y. Du, W. Zhuang, Y. Qi. 2015. Correlation between subsurface high-salinity water in the northern South China Sea and the North Equatorial Current–Kuroshio circulation system from HYCOM simulations. Ocean Sci. Discuss.: 28 October 2014.

B. J. Hoskins. 1982. The mathematical theory of frontogenesis. Annual Review of Fluid Mechanics Vol. 14:131-151.

B. J. Hoskins, F. P. Bretherton. 1972. Atmospheric Frontogenesis Models: Mathematical Formulation and Solution. Journal of the Atmospheric Sciences Volume 29: Issue 1.

Chau-Ron Wu, Ping-Tung Shaw, Shenn-Yu Chao. 1998. Seasonal and interannual variations in the velocity field of the South China Sea. Journal of Oceanography, Vol. 54, pp. 361 to 372.

Clément de Boyer Montégut, Gurvan Madec, Albert S. Fischer, Alban Lazar, Daniele Iudicone. Mixed layer depth over the global ocean: An examination of profile data and a profile-based climatology. Journal of Geophysical Research Volume109, Issue C12.

Xiaolong Yu, Alberto C. Naveira Garabato, et al. 2019. An Annual Cycle of Submesoscale Vertical Flow and Restratification in the Upper Ocean. Journal of Physical Oceanography Volume 49: Issue 6.

David T. Sandwell, Walter H. F. Smith. 1997. Marine gravity anomaly from Geosat and ERS 1 satellite altimetry. Journal Of Geophysical Research, Vol. 102, No. B5, Pages 10,039-10,054, May 10.

Feng Nan, Zhigang He. Hui Zhou, Dongxiao Wang. 2011. Three long-lived anticyclonic

eddies in the northern South China Sea. Journal of Geophysical Research.

Gengxin Chen, Yijun Hou, Qilong Zhang, Xiaoqing Chu. 2010. The eddy pair off eastern Vietnam: Interannual variability and impact on thermohaline structure. Continental Shelf Research Volume 30, Issue 7.

Gengxin Chen, Yijun Hou, Xiaoqing Chu. 2011. Mesoscale eddies in the South China Sea: Mean properties, spatiotemporal variability, and impact on thermohaline structure. Journal of Geophysical Research.

Guimei Liu, Fei Chai. 2009. Seasonal and interannual variability of primary and export production in the South China Sea: a three-dimensional physical–biogeochemical model study. ICES Journal of Marine Science.

Hao Luo, Annalisa Bracco, Yuley Cardona, James C. McWilliams. 2016. Submesoscale circulation in the northern Gulf of Mexico: Surface processes and the impact of the freshwater river input. Ocean Modelling Volume 101.

Hersbach et al. 2020. The ERA5 global reanalysis. Quarterly Journal of the Royal Meteorological Society.

Hideo Nitani. 1972. Beginning of the Kuroshio. The Kuroshio. University of Washington Press, 129–163.

H.L.Varona Gonzalez, D.Veleda, M.Silva, M.Cintra, M.Araujo. 2018. Amazon River plume influence on Western Tropical Atlantic dynamic variability. Dynamics of Atmospheres and Oceans Volume 85, Pages 1-15.

James C McWilliams. 2016. Submesoscale currents in the ocean. Proceedings of the Royal Society A: Mathematical, Physical, and Engineering Sciences. 472: 20160117. PMID 27279778 DOI: 10.1098/rspa.2016.0117.

Jianyu Hu, Hiroshi Kawamura, Huasheng Hong, Yiquan Qi. 2000. A Review on the Currents in the South China Sea: Seasonal Circulation, South China Sea Warm Current and Kuroshio Intrusion. Journal of Oceanography.

Jianping Gan, H. Li, E. N. Curchitser, D. B. Haidvogel. 2006. Modeling South China Sea circulation: Response to seasonal forcing regimes. Journal of Geophysical Research 111, C06034, doi:06010.01029/02005JC003298.

Joachim W Dippner, Nguyen Ngoc Lam, Doan Nhu Hai, Ajit Subramaniam. 2011. A

Model for the Prediction of Harmful Algae Blooms in the Vietnamese Upwelling Area. Harmful Algae.

Jonathan Gula, M. Jeroen Molemaker, James C. McWilliams. 2016. Submesoscale Dynamics of a Gulf Stream Frontal Eddy in the South Atlantic Bight. Journal of Physical Oceanography Volume 46: Issue 1.

Klaus Wyrtki. 1961. Physical oceanography of the southeast Asian waters. NAGA Report 2. San Diego: eScholarship Repository, Scripps Institute of Oceanography, University of California.

Laurent Debreu, Patrick Marchesiello, Pierrick Penven, Gildas Cambon. 2012. Two-way nesting in split-explicit ocean models: Algorithms, implementation and validation. Ocean Modelling Volumes 49–50, June 2012, Pages 1-21.

Leif N. Thomas, Terrence M. Joyce. 2010. Subduction on the Northern and Southern Flanks of the Gulf Stream. Journal of Physical Oceanography Volume 40: Issue 2.

Liu Zhengyu, Yang Haijun, Liu Qinyu. 2001. Regional dynamics of seasonal variability in the South China Sea. Journal of Physical Oceanography, 31: 272–284.

Patrick Marchesiello, Laurent Debreu, Xavier Couvelard. 2009. Spurious diapycnal mixing in terrain-following coordinate models: The problem and a solution. Ocean Modelling Volume 26, Issues 3–4, 2009, Pages 156-169.

Ping-Tung Shaw, Shenn-YuChao. 1994. Surface circulation in the South China Sea. Deep Sea Research Part I: Oceanographic Research Papers.

Quanan Zheng, Jianyu Hu, Benlu Zhu, Ying Feng, Young-Heon Jo, Zhenyu Sun, Jia Zhu, Hongyang Lin, Junyi Li, Ying Xu. 2014. Standing wave modes observed in the South China Sea deep basin. Journal of Geophysical Research.

Roy Barkan, James C. McWilliams, Alexander F. Shchepetkin, M. Jeroen Molemaker, Lionel Renault, Annalisa Bracco, Jun Choi. 2017. Submesoscale Dynamics in the Northern Gulf of Mexico. Part I: Regional and Seasonal Characterization and the Role of River Outflow. Journal of Physical Oceanography Volume 47: Issue 9.

Sarah C. Weber, Ajit Subramaniam, Joseph P. Montoya, Hai Doan-Nhu, Lam Nguyen-Ngoc, Joachim W. Dippner, Maren Voss. 2019. Habitat Delineation in Highly Variable Marine Environments. Frontiers in Marine Science.

Shang-Ping Xie, Chueh-Hsin Chang, Qiang Xie, Dongxiao Wang. 2007. Intraseasonal variability in the summer South China Sea: Wind jet, cold filament, and recirculations. Journal of Geophysical Research, Vol. 112, C10008.

Shenn-Yu Chao, Ping-Tung Shaw, Sunny Y. Wu. 1996. Deep water ventilation in the South China Sea. Deep Sea Research Part I: Oceanographic Research Papers.

Sol Hellerman, Mel Rosenstein. 1983. Normal Monthly Wind Stress Over the World Ocean with Error Estimates. Journal of Physical Oceanography.

Tangdong Qu. 2000. Upper-Layer Circulation in the South China Sea. Journal of Physical Oceanography Volume 30: Issue 6.

Thomas B. Wild, Daniel P. Loucks. 2015. Mitigating Dam Conflicts in the Mekong River Basin. Conflict Resolution in Water Resources and Environmental Management.

Wei Zhuang, Yan Du, Dongxiao Wang, Qiang Xie, Shang-Ping Xie. 2010. Pathways of Mesoscale Variability in the South China Sea. Chinese Journal of Oceanology and Limnology 28(5):1055-1067.

Wendong Fang, Guohong Fang, Ping Shi, Qizhou Huang, Qiang Xie. 2002. Seasonal structures of upper layer circulation in the southern South China Sea from in situ observations. Journal of Geophysical Research, Volume107, Issue C11.

X. Capet, James C. McWilliams, M. J. Molemaker, A. F. Shchepetkin. 2008. Mesoscale to Submesoscale Transition in the California Current System. Part III: Energy Balance and Flux. Journal of Physical Oceanography Volume 38: Issue 10.

Xie Shang-Ping, Xie Qiang, Wang Dongxiao. 2003. Summer upwelling in the South China Sea and its role in regional climate variations. Journal of Geophysical Research, 108(C8):3261.

Xu, X., Z. Qiu, H. Chen. 1982. The general descriptions of the horizontal circulation in the South China Sea, In Proc. Symp. Chin. Soc. Mar. Hydrol. Meteorol. Science Press, Beijing, 119-127.

Yadu Pokhrel, Sanghoon Shin, Zihan Lin, Dai Yamazaki, Jiaguo Qi. 2018. Potential Disruption of Flood Dynamics in the Lower Mekong River Basin Due to Upstream Flow Regulation. Scientific Reports.

Yi Fan, Ke Fan, Zhiqing Xu, Shuanglin Li. 2018. ENSO–South China Sea Summer Monsoon Interaction Modulated by the Atlantic Multidecadal Oscillation. Journal of Cliamte https://doi.org/10.1175/JCLI-D-17-0448.1.

Yuichiro Yoshida, Han Soo Lee, Bui Huy Trung, Hoang-Dung Tran, Mahrjan Keshlav Lall, Kifayatullah Kakar, Tran Dang Xuan. 2020. Impacts of Mainstream Hydropower Dams on Fisheries and Agriculture in Lower Mekong Basin. Sustainability.

Yuley Cardona, Annalisa Bracco. 2012. Enhanced vertical mixing within mesoscale eddies due to high frequency winds in the South China Sea. Ocean Modelling 42, 1-15.

Zhongya Cai, Jianping Gan. 2017. Formation and Dynamics of a Long-Lived Eddy Train in the South China Sea: A Modeling Study. Journal of Physical Oceanography Volume 47: Issue 11.

Zhou Hui, Yuan Dongliang, Li Ruixiang, Li Ruixiang, He Lei. 2010. The western South China Sea currents from measurements by Argo profiling floats during October to December 2007. Chinese Journal of Oceanology and Limnology Vol. 28 No. 2, P. 398-406, 2010.